Original Article

Design and development of a durable series elastic actuator with an optimized spring topology

Mehmet C Yildirim[1], Polat Sendur[2] , Ahmet Talha Kansizoglu[2],
Umut Uras[3], Onur Bilgin[2], Sinan Emre[2], Guney Guven Yapici[2] ,
Mehmet Arik[2] and Barkan Ugurlu[2]

Abstract

This paper aims to present the integrated design, development, and testing procedures for a state-of-the-art torsion-based series elastic actuator that could be reliably employed for long-term use in force-controlled robot applications. The main objective in designing the actuator was to meet weight and dimensional requirements whilst improving the long-term durability, ensuring high torque output, and containing its total weight. A four-fold design approach was implemented: (i) following recursive design-and-test procedures, an optimal torsional spring topology was unveiled with the help of SIMP (Solid Isotropic Material with Penalization) topology optimization method, (ii) the proposed spring was manufactured and multiple specimens were experimentally tested via a torsional test machine to validate linearity, loading rate response, and mechanical limits, (iii) the actuator's thermal response was experimentally scrutinized to ensure that the generated heat was dissipated for long-term use, and (iv) the fatigue life of the spring was computed with the help of real-life experiment data. Having concluded the development and verification procedures, two different versions of the actuator were built, and preliminary torque control experiments were conducted. In conclusion, favorable torque tracking with a bandwidth of 19 Hz was achieved while peak-to-peak torque input was 20 Nm.

Introduction

Physical human-robot interaction (pHRI) has become one of the central topics in contemporary robotics research as a result of the paradigm shift from industrial to service robots. This research field aims to ensure that the robots could leave well-controlled laboratory environments to be used as human companions in a dynamic human environment. In order to realize this goal in a safe and dependable manner, one major requirement is the capability of force sensing and control.[1]

To address the high-fidelity force control requirement in pHRI, researchers proposed torque-controlled actuators in various forms. A straightforward approach is to deploy a torque sensing element, e.g. strain-gauges, to read the output torque,[2] or to employ flexible material between the actuator and the output to measure the applied torque via deflection readings.[3] Pneumatic systems, SEAs (Series Elastic Actuators), PEAs (Parallel Elastic Actuators), series-parallel elastic actuators, and VIAs (Variable Impedance Actuators) are other successful actuator types that allow high fidelity torque sensing and control via intrinsic physical compliance.[4,5]

While the diversity of torque-controlled actuators enabled a series of successful pHRI implementations, only a certain portion of them fulfill the challenging requirements, such as enhanced torque/mass ratio,

[1]Chair of Robotics and Systems Intelligence, Technical University of Munich (TUM), Munich, Germany
[2]Department of Mechanical Engineering, Ozyegin University, Istanbul, Turkey
[3]Department of Mechanical Engineering, Villanova University, Villanova, PA, USA

Corresponding author:
Barkan Ugurlu, Biomechatronics Laboratory, Department of Mechanical Engineering, Ozyegin University, Istanbul 34794, Turkey.
Email: barkan.ugurlu@ozyegin.edu.tr

practicality, structural integrity and mobility. To this end, state-of-the-art SEA units respond well to these criteria, as they are the primary choice for contemporary industrial manipulators,[6] disaster-response humanoids[7] and rehabilitation robots.[8] This led to the development of numerous SEA modules with various design methodologies.[9–11]

In designing the state-of-the-art torsion-based SEAs, researchers follow an FEA-based (Finite Element Analysis) topology design and test procedures. Mostly, the stiffness of the spring is computationally obtained and then tested within the actuator. While useful in its own functionality domain, this practical approach may have the following shortcomings: (i) the elastic and plastic working regions of the springs cannot be explicitly determined, (ii) sole implementation of computational methods may provide misleading results in terms of the stiffness value and spring linearity, (iii) fatigue life of the spring is not determined and often neglected. Moreover, tight mechanical integration with no thermal management in SEA modules may prevent the dissipation of the generated heat in a feasible manner; therefore, active cooling systems are integrated, further increasing the weight and complexity.

In response to the aforementioned missing blocks in SEA development procedures, we propose an integrated design methodology that consists of the following novel contributions: (1) The spring topology was optimized by considering the target stiffness, weight, and manufacturability criteria, (2) Multiple spring specimens were experimentally characterized using a torsional test machine to check linearity, elastic/plastic region boundaries, actual stiffness value, and loading rate response, (3) Fatigue life of the spring was deterministically obtained using the actual loading data, collected from exoskeleton-supported walking experiments,[12] (4) Thermal behavior of the actuator was experimentally verified via an infra-red (IR) camera and thermocouples. In this study, two SEA units with different torque outputs were built using the proposed design methodology while intuitively maximizing torque/mass ratio as much as possible. Having manufactured the SEA units, torque control experiments were conducted to demonstrate the practical torque control capability of the system.

An initial version of this research study including simulation results and preliminary break-up tests were presented.[13] The current manuscript significantly expands the research study and reports the complete experimental results. The improvements can be listed as below: (i) an optimization study for the torsional spring topology and further elaborations on the CAD integration, (ii) additional experiments on the spring to analyze the effect of strain-rate, (iii) newly-conducted experiments to analyze the thermal behavior, (iv) improved fatigue analysis based on real life experiment data, (v) newly-conducted torque

control experiments to check the torque tracking capability.

The remainder of this paper is organized as follows. First, the mechanical structure of the SEA is revealed. Following this, the details concerning the spring design, analysis, and test procedures are provided. Subsequently, thermal behavior of the SEA is discussed with the experimental data. Finally, torque control experiments are presented and the paper is concluded.
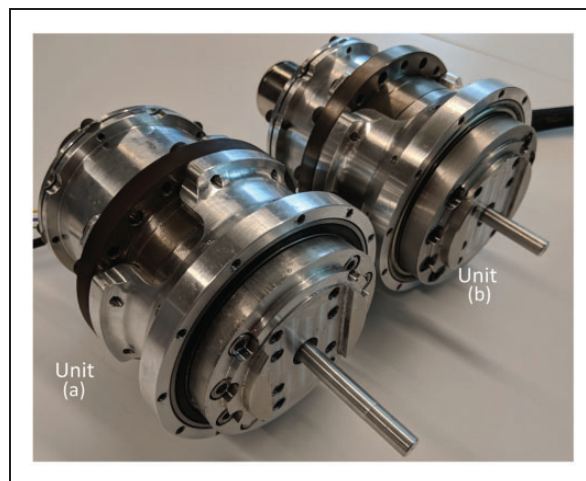
Actuator unit: CoEx-SEA

In order to power exoskeleton robots developed at the Biomechatronics Laboratory of Ozyegin University, two distinct SEA units were developed, namely Compliant Exoskeleton-SEA A & B (CoEx-SEA); see Figure 1. These units consist of three main elements: (i) a frameless brushless DC motor (Kollmorgen TBMs-7631 for the unit A and TBMs-7615 for the unit B), (ii) a low backlash gearbox (Harmonic Drive CSG-25, 1:100 ratio), and (iii) a custom-built torsional spring. Detailed specifications of CoEx-SEA are listed in Table 1.

The CAD view of the design is shown in Figure 2. The gearbox is attached to the torsional spring at the inner circle, whereas the output of the unit is integrated to the spring at the outer circle. CoEx-SEA is also integrated with two 23-bit (Broadcom Avago AS38 H39ES135) absolute encoders which are used to directly measure the motor angle and spring deflection, due to the advantages of encoder-based torque sensing.[14]
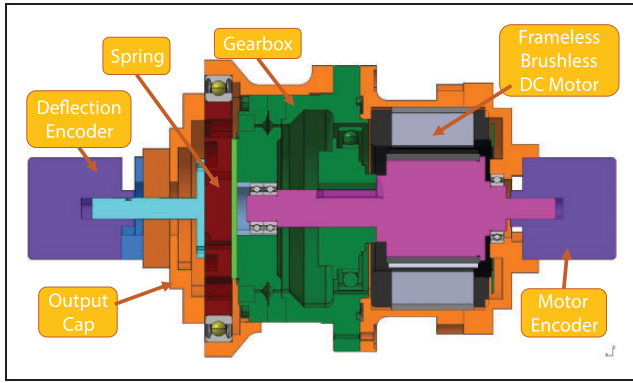
Spring design

In this section, the details of the design methodology are presented. More specifically, topology optimization, experimental verification of the spring, and fatigue life analysis are explained in detail.

Figure 1. Actual CoEx-SEA units, without the deflection encoder and actuator cap.

Table 1. SEA module properties.

Specifications	CoEx-SEA (A)	CoEx-SEA (B)
Max. angular speed (rpm)	26.33	44.09
Max. cont. tor. (Nm)	164	96
Mass (kg)	3.09	2.87
Radius × Length (mm × mm)	53.5 × 132	53.5 × 108
Stiffness (Nm/deg)	80	40
Tor. resolution (mNm)	3.90	3.90
Tor.-to-mass ratio (Nm/kg)	53.07	33.45
Cost (Euro)	≈3700	≈2900

Figure 2. CAD (Computer-aided design) model of the CoEx-SEA unit.

Topology optimization

Design target. Being one of the main elements of the actuator unit, the torsional spring requires a meticulous design process in which the stiffness should be kept linear and the spring should be durable while containing the weight. Therefore the spring was designed by means of an optimization problem with an objective function that minimizes the spring weight and considering the target stiffness as a constraint. A bending based spring structure was adopted due to its favorable characteristic over twist based structures.[10] In our study, the size of the gearbox-motor couple was chosen as the geometric boundary limits for the spring topology.

In defining the spring stiffness, we aimed for a maximum 2° of deflection under a maximum torque load of 164 Nm concerning the unit A. A similar strategy was followed for the unit B. In this regard, softer springs may provide better torque measurement resolution; however, their influence in robot dynamics become more dominant and they limit position control bandwidth.[15] The stiffer springs could be more favorable in this sense; yet, they may greatly limit the measurement quality. Therefore, the design parameter of 2° of deflection under the maximum torque load was determined on the basis of this resolution-accuracy trade-off that we experienced in our earlier works.[15]

Design methodology. Topology optimization requires the design space on which the optimum material distribution will be determined. For this purpose, a design space in the form of a cylinder was defined as shown in Figure 3(a), for which the diameter and the thickness are 80 mm and 10 mm, respectively. As the next step prior to the application of the topology optimization, the location and size of the holes were determined to connect the SEA unit. The stiffness value of a given spring is affected by the connection elements, such as bolts, flanges, insulators. They also increase the spring-related weight. With this in mind, a minimum number of connection elements were targeted in our topology and the spring design in Figure 3(b) was initially obtained. The diameter of the holes was chosen as 8 mm to be consistent with the bolts used. This is the initial geometry for the topology optimization.

Solid Isotropic Material with Penalization (SIMP) topology optimization method was used in this study. In the SIMP approach, material grading is performed by using the relation between relative density variable and material property known as the power law. According to the power-law, or SIMP approach, the relative material density of each discretized element is related to the some power of the material properties of the solid material.[16,17] The objective function of the topology optimization is based on the minimization of the strain energy U as shown in the following

$$h(x) = \min(U(\rho, \theta(\rho))) = \min\left(\int_0^\theta \frac{\tau}{2} d\theta\right) \quad (1)$$

In (1), τ and θ denote torque and twist angle, i.e. torsional deflection, respectively. The topology variable ρ can take a value between 0 and 1; $0 < \rho_{min} < \rho < 1$. The topology optimization algorithm determines the optimum material layout from the initial design space by keeping a certain fraction of the original volume and eliminating the rest. This inequality constraint on the volume ratio is given in the negative null form as below
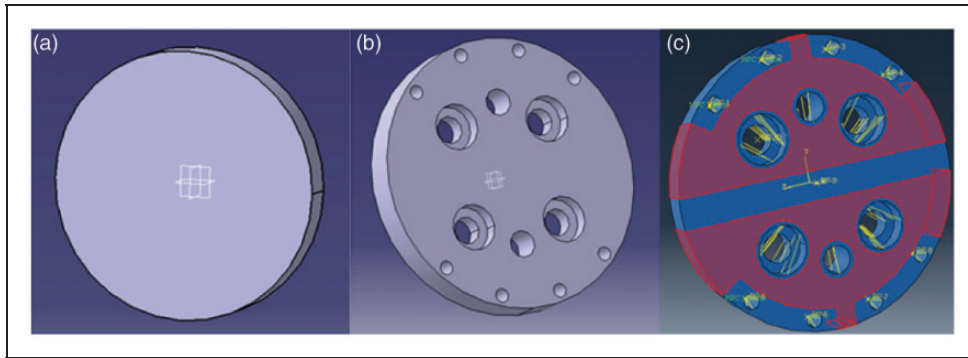
$$\frac{V(\rho)}{V_0} < f \quad (2)$$

where $V(\rho)$, V_0 and f denote the volume, initial volume and the upper limit of the volume ratio, respectively. The equality constraint, shown in (3), represents the linear spring rate of the SEA, K, which is the ratio of the torque and deflection

$$K = \frac{\tau}{\theta} \quad (3)$$

The efficient and accurate determination of the sensitivity is quite important as the derivatives of

Figure 3. (a) Design space, (b) initial design for the topology optimization, (c) design domain (shown in red) and non-design domain (shown in blue).

the objective function and constraints are calculated with respect to thousands of design variables.[18] The sensitivity results are usually obtained in the finite element model.[19] There is also a response surface model approach in the literature to determine the sensitivity, however this method is computationally expensive.[20] To facilitate the design process, we used the embedded sensitivity analysis provided in the topology optimization module of commercial software. Once the sensitivities were calculated, the search direction was determined in accordance with the sensitivity results.

In order to address the aforementioned constraints, a finite element model of the spring was constructed. In this model, the torsional spring was modeled using four-noded tetrahedral elements (C3D4). There are 20,339 finite elements in the model. The aforementioned model was constrained at the inner circle by removing all DOFs. A torque of 180 Nm was given at the spring center to represent the motor torque with an approximately 10% safety factor. The purpose of using 180 Nm torque was to assess the elastic and plastic response of the system under the maximum torque load that can be generated by the motor. To fulfill the lightweight design requirement, aluminum was chosen as the material. 7000 series aluminum alloy (Al-7075) was initially chosen as the grade for its desired fatigue characteristic; see subsection. In the analysis, Poison's ratio, modulus of elasticity, and density of the material were chosen as 0.33, 70 GPa, and 270 kg/m^3, respectively. Static analysis was carried out using Nastran. The results of the analysis were post-processed to calculate the torsional stiffness of the spring by using (3).

In addition to the torsional stiffness, the torque value corresponding to plastic deformation was calculated. For that purpose, the first derivative of the stress-strain curve was calculated and the point on the curve with a negative slope was considered as the yielding point.[21] The finite element model is divided into two parts shown as red and blue regions in Figure 3(c). The material in the area shown in blue color is not included in the topology optimization due to proximity to the connection holes.
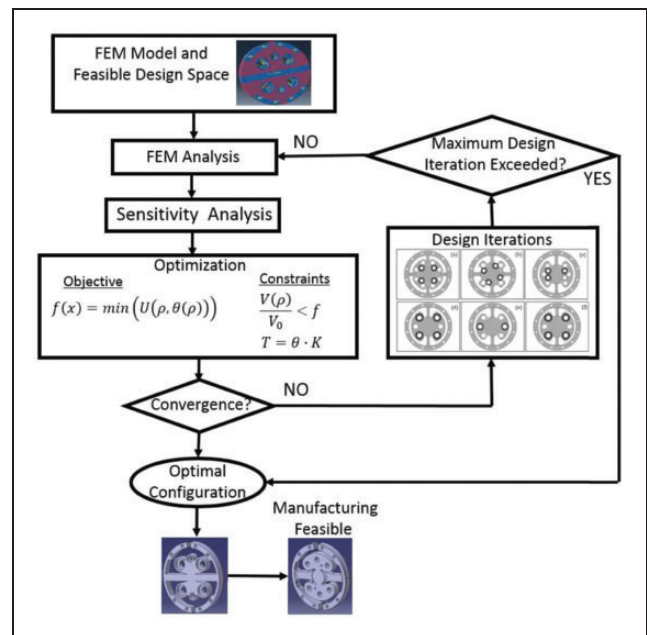
Figure 4. Topology optimization method.

Topology optimization ranks the material shown in red color. The topology optimization methodology is given in Figure 4.

Optimized topology. Optimization algorithm was executed on a PC with Intel® Core™i7-6700 CPU running of 3.4 GHz sampling and 32 GB RAM. The CPU time to complete the optimization run was 30 min. The relative measure of convergence for the design objective was set to 0.1%, meaning that the change on objective function between two subsequent iterations was less than 0.1%. Besides, the maximum number of the iterations was specified to control the overall simulation time and make sure that the optimization does not diverge. The maximum iteration number was set to 200. The critical locations on the initial design was determined by ranking the locations according to the values of the topology variable. Strain energy during the topology optimization is plotted against number of iterations in Figure 5.

The result indicates that the objective function converged in 154 iterations. Furthermore, the volume ratio appeared to be 0.56, meaning that 44% of the material was removed from the initial CAD geometry. Evolution of the topology results can be viewed for various iterations in Figure 6 and also in the multimedia attachment.

One of the disadvantages of the SIMP based topology optimization method is the need for the smooth representation of the optimized topology design. This drawback mainly occurs due to the interpolation of the material densities from the topology optimization results. The aforementioned smooth representation is usually obtained via an iterative process where the designer interprets the topology results and combines them with the computer-aided design and manufacturing processes. Afterward, the design modified according to these constraints is re-analyzed to ensure that the design objective is met.

In this study, once the CAD drawing of the design according to manufacturing constraints was prepared, the finite element analysis was performed. The strain energy distribution was carefully investigated and the region of the design with high strain energy was manually smoothened to reduce the stress

concentration in the geometry. Meantime, the spring deflection value of the SEA unit was monitored to make sure that stiffness target was still realized. Since the stress concentrations are usually related to the local features, they do not affect the overall stiffness. However, making the design iterations with these considerations, the smoothening was completed more efficiently. It was also made sure that the results were not sensitive to the finite element discretization in terms of the type and mesh size of the element used in the finite element model. For example, a finer mesh was used at certain locations where critical design features exist. Besides, the triangular elements are avoided in the regions with high stress concentrations.

Considering the simplicity of the SEA unit, the smoothing of the topology optimization results was performed manually in this study. However, the integration of the manufacturing constraints from different manufacturing methods such as casting, machining, forging, additive manufacturing to the optimization process has been the focus of the researchers recently. The reader is referred to the work of Chen et al. for the direct generation of the design from topology optimization.[22]

The refined manufacturable design and the von-Mises stress distribution from the static analysis is shown in Figure 7. The results of the static analysis indicated that the maximum torsional deflection of the new design was $1.7°$ compared to the design target of $2°$. The difference was attributed to the conversion from the topology results to a more manufacturable design. The refined manfacturable design and von-Mises stress distribution from the static analysis is displayed in Figure 7. With this final design, the maximum stress of $435 \, \text{MPa}$ at the $2°$ of torsional deflection was achieved.
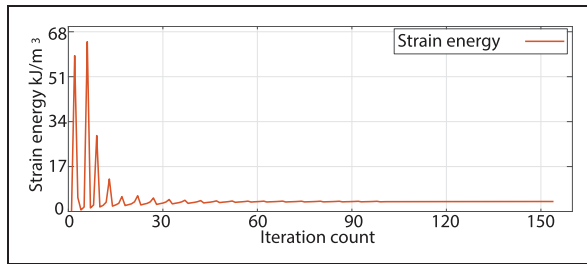
Figure 5. Strain energy variation during the optimization process.
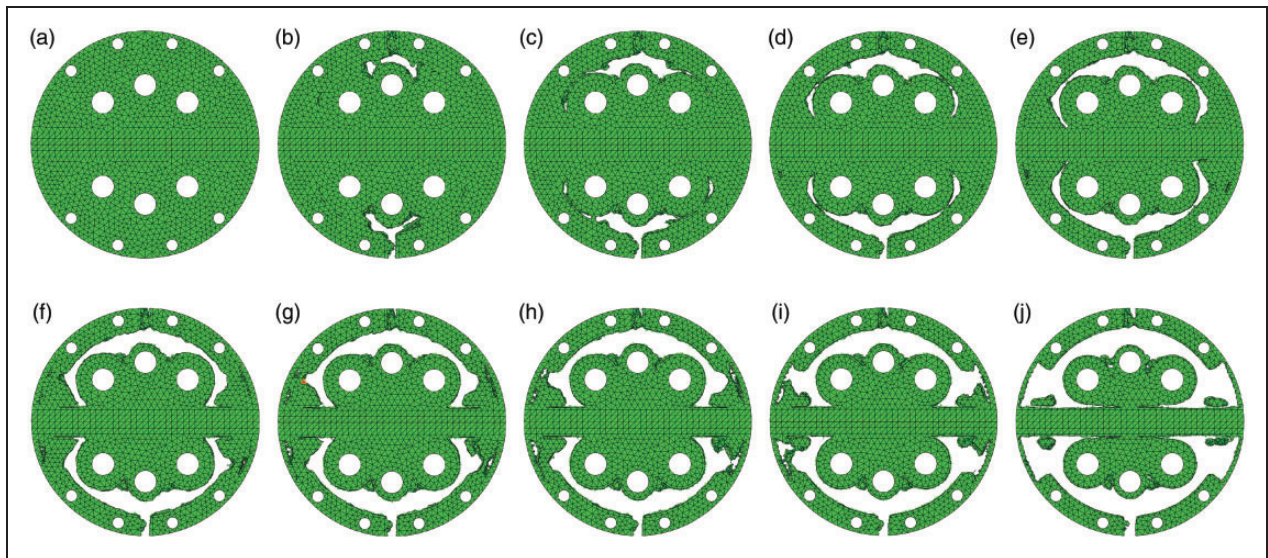
Figure 6. Spring topology evolution during the optimization iterations. After last iteration, manual modifications were carried out to finalize the manufacturable design.
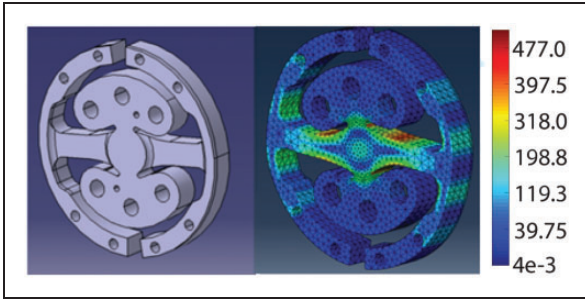
Figure 7. Topology optimization results (left) and von-Mises stress distribution, displayed via colored bars (right).

Figure 8. Stiffness test results, experiment data versus FEA.

In addition, it is observed that the spring stiffness may be adjusted by effectively arranging spring thickness (δ_s) and feder thickness (δ_f) values. 52 finite element models with distinct spring and feder thickness values were simulated. The results of this parametric study were used to derive empirical formulae between design parameters (δ_s and δ_f) and spring stiffness. More specifically, the coefficients of the empirical formula were computed via a least-squares method by using Matlab's nonlinear least squares solver, lsqcurvefit.[23] Due to its favorable correlation performance confirmed via simulations, a quadratic empirical equation was chosen as given in (4) and (5) for the stiffness and yield torque representations, respectively. The comparison between the empirical formula and finite element simulation results shows that the maximum relative error is less than 1.5%, adequately validating the parametrization study

$$k_{EMP} = -8.5 - 0.34\delta_s^2 + 0.52\delta_f^2 + 3.42\delta_s \\ -4.34\delta_f + 1.03\delta_s\delta_f \tag{4}$$

$$\tau_{EMP} = -184.15 - 1.45\delta_s^2 - 0.63\delta_f^2 + 29.99\delta_s \\ +18.27\delta_s + 0.71\delta_s\delta_f \tag{5}$$

Experimental verification of the spring

The spring was experimentally verified via a Torsional Test Machine (TTM). An identical specimen was connected to TTM with two high-stiffness custom made connector to avoid coupling effects.[13] Three main experiments were performed on the specimen: stiffness test, break-up test, and strain rate test. While the break-up and strain rate tests were to understand the fundamentals of the spring, stiffness test was used to assess the stiffness of the spring and validate the FEM results. In the break-up test, the plastic characteristics of the spring was identified.

Stiffness test. In the stiffness test, it is ensured that the stress on the torsional spring is lower than the yield strength. The comparison between the test and the prediction of the finite element model is displayed in Figure 8. The relative error between the simulation
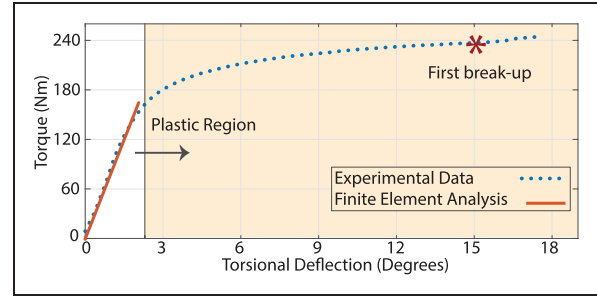
and experimental data was calculated to quantify the accuracy of the FEM model. The results showed that the maximum relative error on the stiffness is 6.5% in the elastic region. Similarly, the average relative error between simulation and experimental data was 4.8%. The results indicated high correlation, especially for the torque values lower than 148 Nm. It was also confirmed that the design requirements were met since the stresses were in the elastic region. The design target on torsional stiffness of 80 Nm/deg was also achieved. Therefore, we observe that the spring can be used as a torque sensor to measure the torque accurately with a nonlinearity error of 5% up to 148 Nm, 90% of the maximum output torque. Around the maximum torque output, the nonlinearity error reached to its maximum 13%; yet, it can be decreased to 0.85% over the entire range via a cubic polynomial fit.

Break-up test. In this test, the torque input was gradually increased until the spring failed. Therefore we could determine the instant at which the spring transitions from elastic to plastic region. Plastic deformation of the spring is shown in Figure 9.

As it may be seen in Figure 8, the transition from elastic to plastic characteristics occurred at the angular deflection of 2°. After this angular deflection value, the first break-up was observed when the applied torque was 240 Nm; see Figure 8. Since this amplitude is considerably more than the torque output capability of CoEx-SEA, the designed spring is deemed to be suitable for our applications. See Figure 9 for the broken specimens after the break-up experiments.

Strain rate test. In order to account for the frequency dependency of the torque loading, we considered the effect of loading frequency of the spring unit in this section. It is known in the literature that frequency range of torque loading is quite broad.[12,13,24] Our initial simulation and experimental results indicate that the control bandwidth can be enlarged as high as 25 Hz.[25] Results of finite element analysis showed that the main deflection characteristics of the spring unit are mainly related to the Young's modulus of the material. In this
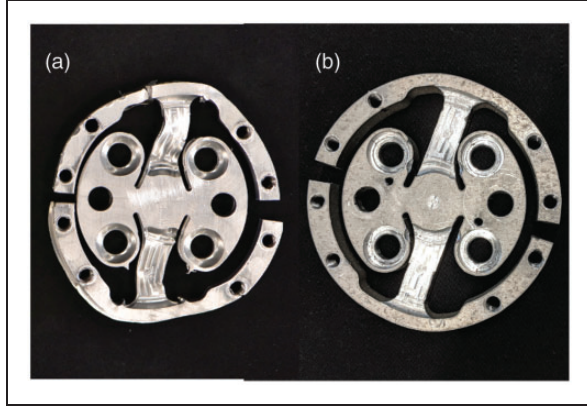
Figure 9. Tested springs after break-up experiments with different maximum loading rates. Each specimen loaded with same maximum loading and up to 130% of their yielding torque values.

study, we used the stress-strain relation given in[21] to analyze the frequency of the torque loading effect

$$\sigma = C\dot{\epsilon}^m \qquad (6)$$

where m, C, and ϵ denote strain rate sensitivity, material constant and, strain rate, respectively. Due to the limitation of the loading rate of the TTM, we followed the methodology provided in[21] to consider the effect of higher frequencies. The essence of this method is to use the difference of two stress values corresponding to two different loading rates for calculating the strain rate sensitivity. For this purpose, two aluminum 7000 series specimen with feder thickness of 7.0 mm and spring thickness of 7.0 mm were tested in TTM under the two limiting loading rates: 1 mm/deg and 5 mm/deg. The strain rate is the calculated as below

$$m = \frac{ln(\tau_2/\tau_1)}{ln(\dot{\theta}_2/\dot{\theta}_1)} \qquad (7)$$

In (7), the subscripts 1 and 2 represent the loading rate of 1 mm/deg and 5 mm/deg, respectively. We selected five different torque values ($\Delta\tau$) and calculated the sensitivity rate using equation (7). Once m is determined, the same equation is used to extrapolate the response for the spring unit at higher loading rates. Torque vs angle is plotted for the loading rates of 0.5 Hz, 1 Hz, 10 Hz, and 25 Hz in Figure 10.

Fatigue life

Having determined the stiffness characteristics and elastic/plastic limits, we assessed the fatigue life of the spring using the methodology depicted in Figure 11. For this analysis, rather than considering constant-valued torques, e.g.,[26] we made use of the experimental torque data provided from the real-life exoskeleton-supported walking experiments.[12]
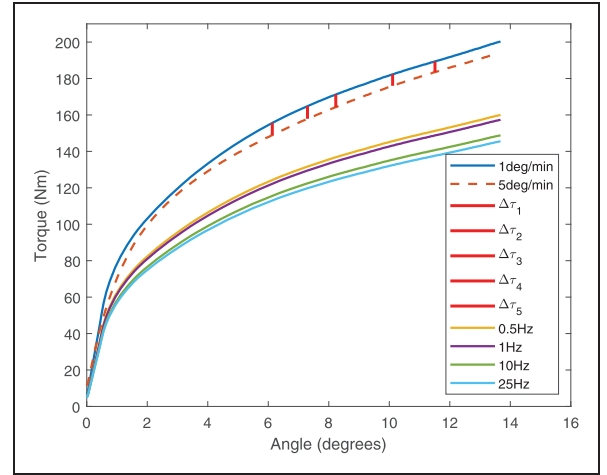
Figure 10. Experimental results on strain rate at different loading speeds (1 deg/min and 5 deg/min), randomly chosen torque differences between different loading rates for the same deflection values ($\Delta\tau_1 - \Delta\tau_5$). Forecasts for the higher loading rates rate (0.5–25 Hz).
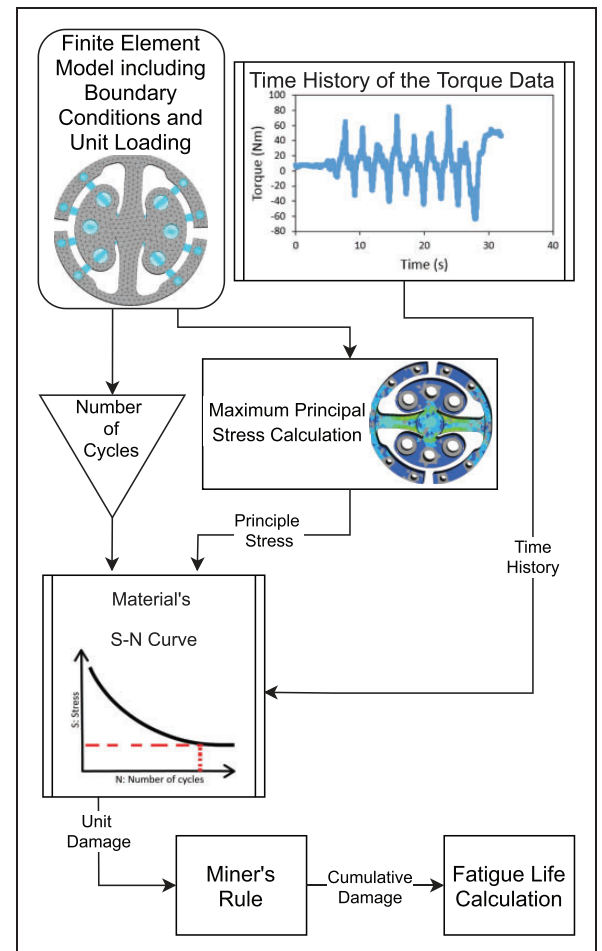
Figure 11. Fatigue life calculation methodology.

Finite element model of the SEA including the boundary conditions was analyzed under unit torque. The fatigue strength of the Al-7075 is 159 MPa under 5.10^8 completely reversed stress

cycles.[27] The maximum principal stress was used in the fatigue life prediction of our model. The Palmgreen-Miner cumulative fatigue damage theory, also known as Miner's Rule, was used to determine the fatigue life for SEA module[28] as follows, under the operational loading provided in.[12] In accordance with the Miner's Rule, accumulated damage was calculated as below

$$C = \frac{n_1}{N_1} + \frac{n_2}{N_2} + \cdots + \frac{n_i}{N_i} \qquad (8)$$

where n_i and N_i represent the cycle numbers corresponding to the *ith* stress level and failure, respectively. n_i/N_i is known as the damage ratio at the *ith* stress level. The parameter C is taken as unity corresponding to failure.[28] The proposed fatigue life calculation methodology is implemented in Matlab software to determine the fatigue life for a given time history of the torque data.

The stress distribution from the FEA result represent an almost fully reversible stress state. Since most of the S-N data is only applicable for completely reversed stress, the standard S-N curve was directly used to relate the strength to the number of cycles to failure. For the stress distribution with non-zero mean stress, additional correction methods such as Goodman and Gerber are needed. An equivalent completely reversed stress that is expected to be as damaging as the fluctuating stress is needed under those circumstances. The reader may refer to additional stress correction methods for more detailed information.[29] The geometry of the SEA spring is iteratively modified to reduce the stress concentration factors. The maximum von-Mises stress corresponding to the final design is 172 MPa. The distribution of the damage profile corresponding to the loading is shown in Figure 11. The maximum fatigue damage occurs on the inner radius of the part with a damage value of $2.2 \cdot 10^{-7}$. Therefore, the loading could be applied for $1/(2.2 \cdot 10^{-7}) = 4.55 \cdot 10^{6}$ cycles. Since one cycle of the torque data is 32 s, this corresponds to about 97,916 h of operation (1,579 days) for the aforementioned experiment.

It must be noted that the fatigue analysis is of crucial importance when designing components that are supposed to perform long-term tasks. For instance, a spring made out of 6000 Aluminum with exactly the same topology would respond similarly for finite element analysis and experimental break-up tests. Yet, its fatigue life is approximately 79 days given the operational loading. This is expected because all the parameters remain the same except the yield torque. Therefore, a spring design with no fatigue analysis may not guarantee long-term service.

The Miner's rule is a linear damage model. The use of Miner's rule is common and still recommended in the literature.[30] The main assumption of the Miner's

rule is that the damage accumulation is independent of the load conditions and sequences. Considering the linear characteristics of the SEA unit up to almost 150 N.m as shown in Figure 8, the Miner's rule is deemed sufficient for the calculation of the fatigue life of our SEA unit. There are many fatigue damage accumulation methods which are based on nonlinear accumulation laws in the literature.[31] For more accurate fatigue life calculation, those nonlinear damage models can be easily integrated to the proposed design development methodology.

Thermal analysis

Considering the physical robot-human interaction, the thermal behavior of the SEA unit plays an important role. Moreover, the increased temperature within the unit may cause performance degradation. To this end, many researchers proposed active cooling systems.[9,32] The existing literature also shows that actuation units used in robotics can reach high temperatures in a short process time,[32] which may deteriorate the actuator performance. In order to address these design requirements, we used the experimental method proposed in.[33] The experimental setup and hardware used in the experiments are shown in Figure 12.

A Flir SC5000 IR camera with a wavelength range of 2.5 μm–5.1 μm and sensitivity up to $20 mK$ was employed. The measurement system had an accuracy of 1% for temperatures less than 15 °C. In addition, a data acquisition device (Agilent 34972 A LXI) with T-type thermocouples was used to verify the data collected from the IR camera. The accuracy of the aforementioned thermocouples is 1 °C. Prior to the experiments, the SEA module was painted in black with an emissivity of 0.98 for all components to have the same emissivity level. An IR thermography software was calibrated with respect to this emissivity level. Due to the high heat transmission capacity of
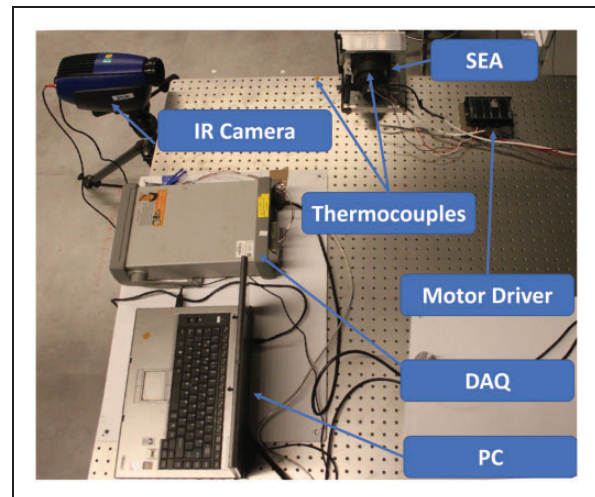
Figure 12. Experimental setup for the thermal investigations.

the aluminum, the temperature difference between the motor and the outer surface of the actuator could be neglected. The measurements between the thermocouple and IR camera were highly correlated. The maximum relative error was 1.8%, while the average relative error was only 0.5%.

With a 12.5 kg load, aforementioned walking torque profile is mimicked. Figure 13 depicts the 3D temperature plot of the actuator unit after 30 s and 19 min. In addition, it displays the IR camera images from the corresponding moments. These results indicate that the heat transfer between the heat generating parts (motor, encoder, etc.) and the other components of the SEA module was not significant. This finding was verified by comparing the data collected from thermocouples and IR thermography; see Figure 14.

Having repeated the tests for several trials with the safety of the experimental setup in mind, the thermal response of the system was modeled considering Newton's law of cooling

$$T(t) = T_c + (T_o - T_c)e^{-dt} \qquad (9)$$

In (9) $T_c = 34.3°C$, $T_o = 24.0°C$, and $d = 0.03988\,s^{-1}$. This model shows that the temperature of the SEA where it is in close proximity to the human-user will converge to a maximum value of $34.3°C$, which is sufficiently lower than that of the maximum suggested operation temperature limit of our brushless DC motor.

Torque control implementation

In order to verify the torque control capability of the proposed SEA system, we conducted torque control experiments using a test bench powered via CoEx-SEA(A) unit. A uniform link with a mass of 1.2 kg and a length of 42 cm was attached as the mechanical output. As a payload, a 5-kg dumbbell was used at the tip. As the controller, a sliding mode with a disturbance observer method proposed in[34] was utilized due its favorable characteristics, e.g. robustness, reduced chattering and high fidelity tracking.
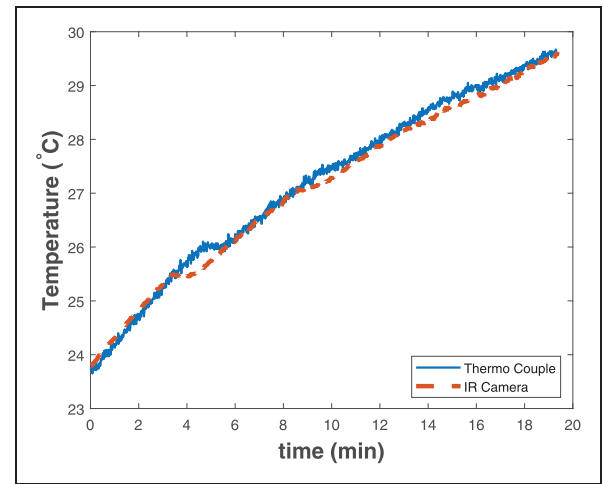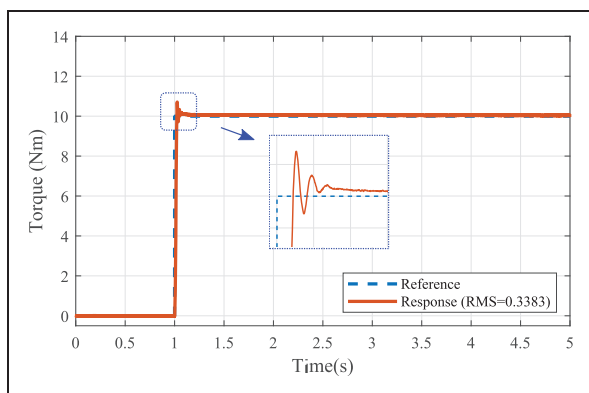

Figure 14. Temperature data of the SEA for 19 min.
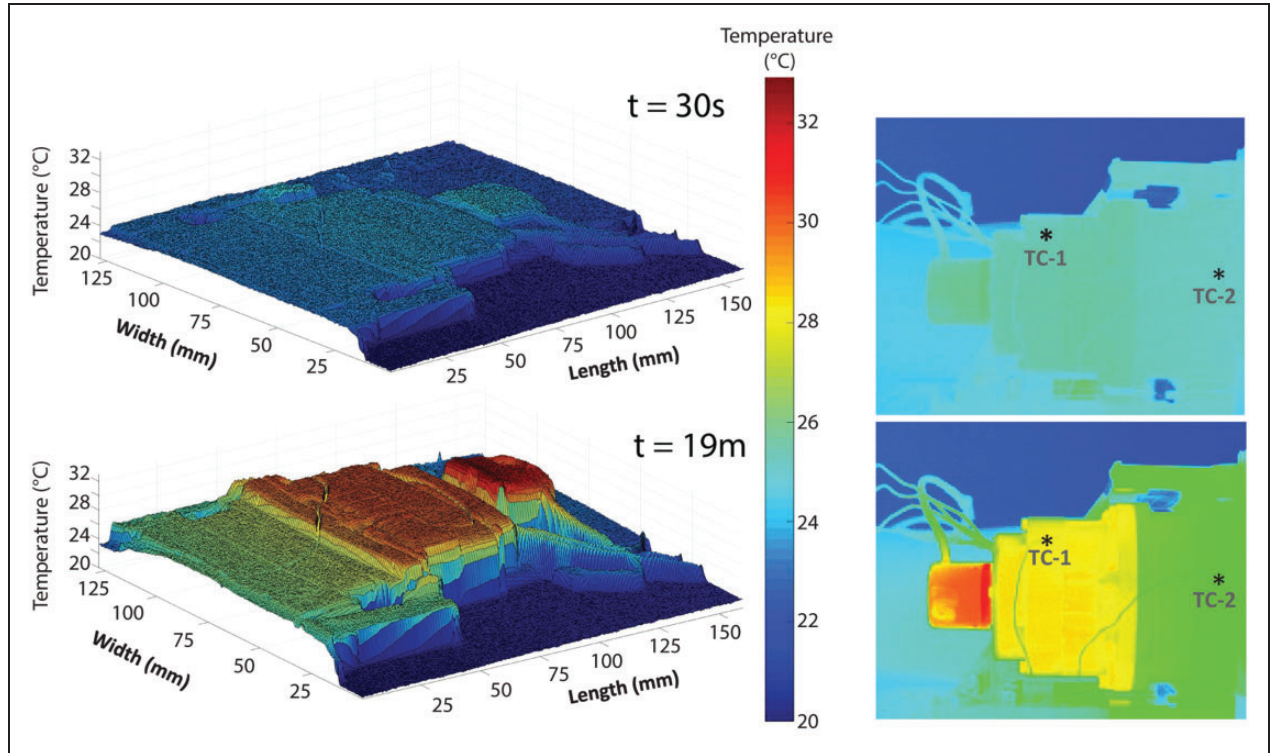
Figure 13. 3D temperature plot of the actuator at $t = 30s$ and $t = 19min$. The displayed data were taken from the first thermocouple. The corresponding thermal camera images can also be viewed. Thermocouple locations are indicated as TC-1 and TC-2.
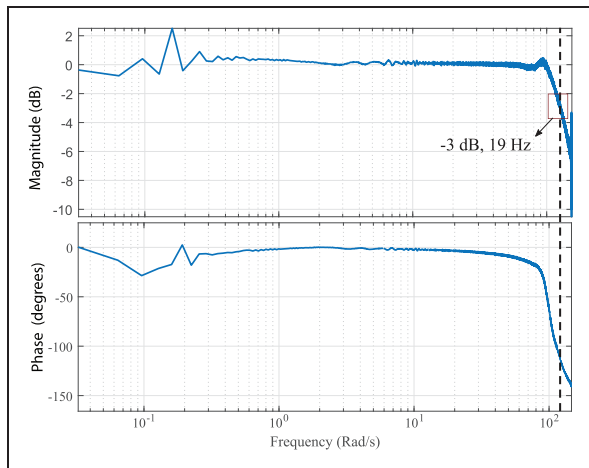
Figure 15. Torque tracking performance for the chirp input, Bode diagram.

Figure 16. Torque tracking performance for the a step input.

To determine the controller bandwidth, a chirp input with a peak-to-peak amplitude of 20 Nm was applied. Using the reference and actual torque measurements, a Bode diagram was constructed; see Figure 15. As may it be observed, the bandwidth of the controller is 19 Hz which is satisfactory when considering the input amplitude. Furthermore, Figure 16 shows the step response of the controller. The solid red and dashed blue lines respectively indicate the torque reference and measurement. It was observed that the torque response exhibited 6% overshoot while settling in less than 0.1 s. The steady-state error was only 0.05 Nm. In light of these results, the torque control capability of the SEA unit was verified. Refer to the multimedia attachment for zero input torque and gravity compensation experiments.

Concluding remarks

This paper presented a systematic design and development methodology that can be referred for the design and testing of torsion-based series elastic actuators. Compared to conventional design and test procedures, it provided a comprehensive road map to cover the important design aspects which are often overlooked in the literature, e.g. optimized spring topology, experimental verification of the spring stiffness together with its elastic/plastic region boundaries, fatigue life of the spring, experimental verification of the thermal behavior concerning the whole unit. Through the integration of these crucial design and test tools, we argue that SEAs could be adapted well to pHRI applications concerning their long-term and repetitive use.

The proposed methodology was implemented for the design of two high power SEA units with distinct torque output capabilities. A special emphasis was given to mechanical integration of the units to satisfy dimensional and weight requirements while containing the weight. To demonstrate the torque control capability, a series of experiments were conducted. As a result, we obtained satisfactory tracking results both for high and low-frequency torque reference inputs, adequately confirming the usability of the system. Currently, we built 11 samples of these units to actuate our exoskeleton systems which will be reported in our future research.

Declaration of Conflicting Interests

The author(s) declared no potential conflicts of interest with respect to the research, authorship, and/or publication of this article.

ORCID iDs

Polat Sendur https://orcid.org/0000-0003-2212-7419
Guney Guven Yapici https://orcid.org/0000-0001-5692-4809
Barkan Ugurlu https://orcid.org/0000-0002-9124-7441

References

1. Albu-Schaffer A, Eibergerand O, Grebenstein M, et al. Soft robotics. *IEEE Robot Automat Mag* 2008; 15: 20–30.
2. Kim YB, Kim U, Seok DY, et al. Torque sensor embedded actuator module for robotic applications. *IEEE/ASME Trans Mechatron* 2018; 23: 1662–1672.
3. Hau S, Rizzello G, Hodgins M, et al. Design and control of a high-speed positioning system based on dielectric elastomer membrane actuators. *IEEE/ASME Trans Mechatron* 2017; 22: 1259–1267.

4. Ham RV, Sugar TG, Vanderborght B, et al. Compliant actuator designs. *IEEE Robot Automat Mag* 2009; 16: 81–94.

5. Plooij M, Wisse M and Vallery H. Reducing the energy consumption of robots using the bidirectional clutched parallel elastic actuator. *IEEE Trans Robot* 2016; 32: 1512–1523.

6. Fitzgerald C. Developing baxter. In *2013 IEEE Conference on Technologies for Practical Robot Applications (TePRA)*, 22-23 April 2013, pp. 1-6. Woburn: IEEE.

7. Klamt T, Rodriguez D, Baccelliere L, et al. Flexible disaster response of tomorrow. *IEEE Robot Automat Mag* 2019; 26: 59–72.

8. Wang S, Wang L, Meijneke C, et al. Design and control of the mindwalker exoskeleton. *IEEE Trans Neural Syst Rehabil Eng* 2014; 23: 277–286.

9. Kim D, Campbell O, Ahn J, et al. Investigations of viscoelastic liquid cooled actuators applied for dynamic motion control of legged systems. In: *Proceedings of 2017 IEEE-RAS 17th international conference on humanoid robotics*, (Humanoids), Birmingham, UK, pp. 710–717.

10. Negrello F, et al., Design and characterization of a novel high-compliance spring for robots with soft joints. In *2017 IEEE International Conference on Advanced Intelligent Mechatronics (AIM)*, 2017, Munich, Germany, pp. 271–278, doi: 10.1109/AIM.2017.8014029.

11. Herodotou P and Wang S. Design, modelling, and experimental evaluation of a compact elastic actuator for a gait assisting exoskeleton. In: *2019 IEEE 16th international conference on rehabilitation robotics*. (ICORR), 24-28 June, Toronto, Canada, Piscataway: IEEE, pp. 331–336.

12. Ugurlu B, Oshima H and Narikiyo T. Lower body exoskeleton-supported compliant bipedal walking for paraplegics: how to reduce upper body effort? In: *Proceedings of 2014 IEEE international conference on robotics and automation*, (ICRA), Hong Kong, pp. 1354–1360.

13. Yildirim MC, Sendur P, Bilgin O, et al. An integrated design approach for a series elastic actuator: stiffness formulation, fatigue analysis, thermal management. In: *Proceedings of 2017 IEEE-RAS 17th international conference on humanoid robotics*, (Humanoids), Birmingham, UK, pp. 384–389.

14. Kashiri N, Malzahn J and Tsagarakis NG. On the sensor design of torque controlled actuators: a comparison study of strain gauge and encoder-based principles. *IEEE Robot Autom Lett* 2017; 2: 1186–1194.

15. Ugurlu B, Saglia JA, Tsagarakis NG, et al. Bipedal hopping pattern generation for passively compliant humanoids: exploiting the resonance. *IEEE Trans Ind Electron* 2014; 61: 5431–5443.

16. Bendsøe MP. Optimal shape design as a material distribution problem. *Struct Optim* 1989; 1: 193–202.

17. Sigmund O. A 99 line topology optimization code written in matlab. *Struct Multidisc Optim* 2001; 21: 120–127.

18. Paris J, Navarrina F, Colominas I, et al. Stress constraints sensitivity analysis in structural topology optimization. *Comput Methods Appl Mech Eng* 2010; 199: 2110–2122.

19. Bendsøe MP and Kikuchi N. Generating optimal topologies in structural design using a homogenization method. *Comput Methods Appl Mech Eng* 1988; 71: 197–224.

20. Chuang C, Yang R, Li G, et al. Multidisciplinary design optimization on vehicle tailor rolled blank design. *Struct Multidisc Optim* 2008; 35: 551–560.

21. Hosford WF and Caddell RM. *Metal forming: mechanics and metallurgy*. Cambridge: Cambridge University Press, 2007.

22. Chen Y, Lu J and Wei Y. Topology optimization for manufacturability based on the visibility map. *Comput Aided Des Appl* 2016; 13: 86–94.

23. Matlab® optimization toolbox™: User's guide, r2020b. Natick, MA, US Mathworks, Inc., https://www.mathworks.com/help/optim/index.html (accessed: May 25, 2021).

24. Hutter M, Gehring C, Lauber A, et al. Anymal - toward legged robots for harsh environments. *Adv Robot* 2017; 31: 918–931.

25. Kansizoglu AT, Sariyildiz E and Ugurlu B. A comparison study on observer-based force control of series elastic actuators. In: *Proceedings of 2018 IEEE 15th international workshop on advanced motion control (AMC)*, Tokyo, Japan, 9–11 March 2018, pp. 411–416. IEEE.

26. Wang S, Meijneke C and van der Kooij H. Modeling, design, and optimization of mindwalker series elastic joint. In: *Proceedings of 2013 IEEE international conference on rehabilitation robotics (ICORR)*, Seattle, WA, USA, 24–26 June 2013, pp.1–8. Piscataway: IEEE.

27. Oskouei R and Ibrahim R. The effect of a heat treatment on improving the fatigue properties of aluminium alloy 7075-T6 coated with TiN by PVD. *Procedia Eng* 2011; 10: 1936–1942.

28. Miner MA. Cumulative damage in fatigue. *J Appl Mech* 1945; 12: A159–A164.

29. Budynas RG and Nisbett JK. *Shigley's mechanical engineering design*. 10th ed. New York: McGraw-Hill Education, 2014.

30. Schoenborn S, Kaufmann H, Sonsino C, et al. Cumulative damage of high-strength cast iron alloys for automotive applications. *Procedia Eng* 2015; 101: 440–449.

31. Zhu SP, Liao D, Liu Q, et al. Nonlinear fatigue damage accumulation: isodamage curve-based model and life prediction aspects. *Int J Fatigue* 2019; 128: 105185.

32. Ito Y, Nozawa S, Urata J, et al. Development and verification of life-size humanoid with high-output actuation system. In: *Proceedings of 2014 IEEE international conference on robotics and automation (ICRA)*, Hong Kong, China, 31 May–5 Jun 2014, pp. 3433–3438. Piscataway: IEEE.

33. Garg J, Arik M, Weaver S, et al. Micro fluidic jets for thermal management of electronics. In: *Proceedings of ASME 2004 heat transfer/fluids engineering summer conference*, Charlotte, NC, USA, 11–15 July 2004, pp. 647–654. New York: ASME.

34. Sariyildiz E, Yu H, Nozaki T and Murakami T. Robust force control of Series Elastic Actuators using Sliding Mode Control and Disturbance Observer, IECON 2016 – 42nd Annual Conference of the IEEE Industrial Electronics Society, 2016, Florence, Italy, pp. 619–624, doi: 10.1109/IECON.2016.7792991.